International Journal of Solids and Structures 47 (2010) 559–570

Contents lists available at ScienceDirect

International Journal of Solids and Structures

journal homepage: www.elsevier.com/locate/ijsolstr

Mesoscopic model to simulate the mechanical behavior of reinforced concrete members affected by corrosion

P.J. Sánchez [a,c,*], A.E. Huespe [a], J. Oliver [b], S. Toro [c]

[a] CIMEC-INTEC-UNL-CONICET, Güemes 3450, 3000 Santa Fe, Argentina
[b] ETSECCPB, Technical University of Catalonia, Barcelona, Spain
[c] GIMNI-UTN-FRSF, Lavaisse 610, 3000 Santa Fe, Argentina

ARTICLE INFO

Article history:
Received 14 July 2009
Received in revised form 18 September 2009
Available online 1 November 2009

Keywords:
Reinforced concrete structures
Corrosion
Finite elements with embedded strong discontinuities
Bond stress degradation
Contact elements

ABSTRACT

In this contribution, a finite element methodology devised to simulate the structural deterioration of corroded reinforced concrete members is presented. The proposed numerical strategy has the ability to reproduce many of the well-known (undesirable) mechanical effects induced by corrosion processes in the embedded steel bars, as for example: expansion of the reinforcements due to the corrosion product accumulation, damage and cracking patterns distribution in the surrounding concrete, degradation of steel–concrete bond stress transfer, net area reduction in the reinforcements and, mainly, the influence of all these mentioned mechanisms on the structural load carrying capacity predictions.

At the numerical level, each component of the RC structure is represented by means of a suitable FE formulation. For the concrete, a cohesive model based on the Continuum Strong Discontinuity Approach (CSDA) is used. Steel bars are modeled by means of an elasto-plastic constitutive relation. The interface is simulated using contact-friction elements, with the friction degradation as a function of the degree of corrosion attack. Two different (and coupled) mesoscopic analyzes are considered in order to describe the main physical phenomena that govern the problem: (i) an analysis at the cross section level and (ii) an analysis at the structural member level.

The resultant mechanical model can be used to simulate generalized reinforcement corrosion. Experimental and previous numerical results, obtained from the available literature, are used to validate the proposed strategy.

1. Introduction

The economic importance and the technological consequences of the corrosion phenomenon observed in RC elements have motivated, in the last years, numerous research programs. It can be mentioned many experimental works reporting the undesirable corrosion effects on RC elements, see for example (Rodriguez et al., 1994, 1995, 1996; Okada et al., 1988; Uomoto and Misra, 1988; Tachibana et al., 1990; Cabrera and Ghoddoussi, 1992; Almusallam et al., 1996; Al-Sulaimani et al., 1990; Huang and Yang, 1997), and also analytical studies and numerical models (Bazant, 1979a,b; Bhargava et al., 2006, 2007; Vecchio, 2001; Castellani and Coronelli, 1999; Coronelli and Gambarova, 2004; Fang et al., 2006) addressed to understand this complex degradation mechanism.

From the wide spectrum of phenomena involved in the reinforcement corrosion process, in the present work we are only interested in those aspects related with the mechanical problem. In this context, we present a numerical model suitable to simulate the evolution of the mechanical degradation mechanisms of RC structural members caused by the reinforcement corrosion. Phenomena such as: (i) expansion of the corroded bars, (ii) distribution of crack patterns, (iii) loss of steel–concrete bond, (iv) net area reduction of the steel bar cross section and (v) the effects of the above mentioned mechanisms on the structural load carrying capacity, can be analyzed as a function of the reinforcement corrosion degree. Therefore, the model makes possible to determine the influence and sensitivity of this key variable, the reinforcement corrosion level, in the structural deterioration problem.

The proposed numerical strategy can be applied to beams, columns, slabs, etc., through two successive and coupled mesoscopic mechanical analyzes, as follows:

(i) *At the structural member cross section level*, we simulate the reinforcement expansion due to the volume increase of the steel bars as a consequence of corrosion product accumulation. Damage distribution and cracking patterns in the concrete bulk and cover is evaluated, which (indirectly) defines the concrete net section loss in the structural member.

* Corresponding author. Address: CIMEC-INTEC-UNL-CONICET, Güemes 3450, 3000 Santa Fe, Argentina.
E-mail address: psanchez@intec.unl.edu.ar (P.J. Sánchez).

0020-7683/$ - see front matter © 2009 Elsevier Ltd. All rights reserved.
doi:10.1016/j.ijsolstr.2009.10.023

(ii) *A second mesoscopic model at the structural level*, considering the results of the previous analysis, evaluates the mechanical response of the structural member subjected to an external loading system. This evaluation determines the global response and the macroscopic mechanisms of failure.

Simplified models based on limit analysis have been proposed in the literature. They provide, in general, a limited description of the phenomenon involved in the structural response when corrosion effects must be considered. For example, the proposal of Rodriguez et al. (1995), can only provide estimates of the upper and lower bound for the limit loads in a limited number of structural failure modes. Alternatively, numerical simulation models provide a more detailed description of the phenomenology involved in the problem, as also, a more accurate sensitivity evaluation of the corrosion effects on the structural response. Additionally, our present approach has two ingredients which are different respect to previous numerical models, for example that of Coronelli and Gambarova (2004). They are: (i) the above described two coupled mesoscopic analysis, and mainly (ii) the concrete fracture model we use.

Finally, we note one limitation of the present approach that is related with the capturing of the reinforcement maximum strain prediction at failure. This effect is mainly governed by the pitting corrosion phenomenon in the rebar which may be the cause of a premature structural failure. It has not been modeled in the present approach.

The paper is organized as follows. Sections 2 and 3 are devoted to describe the basic ingredients defining both, the mesoscopic cross section and the structural proposed models, respectively. Section 4 presents a consistent coupling between the two mentioned analyzes. Applications of such strategy to determine limit loads in RC beams, as a function of corrosion attack depth, are shown in Section 5. The obtained quantitative structural limit load predictions and qualitative failure modes are compared with available experimental results and other numerical estimation previously proposed. Finally, in the last section, some conclusion are exposed.

2. Cross section analysis of the structural member (expansion mode)

Let us consider the cross section of an arbitrary RC structural member, as displayed in Fig. 1(b), whose reinforcements are experiencing a corrosion process. The products derived from the steel bar corrosion, such as ferric oxide rust, reduce the net steel area and accumulate causing volumetric expansion of the bars (see Fig. 1(a)), what induces a highly hoop tensile stress state in the surrounding concrete. As a consequence the cover concrete undergoes and a degradation process displaying two typical fracture patterns: (i) inclined cracks and (ii) delamination cracks, as observed in Fig. 1(c) (see also Capozucca, 1995). Obviously, these induced cracks can increase the rate of corrosion process in the structural member.

In this Section, we present a numerical model based on a finite element technique that is specially addressed to study this phenomenon. The two-dimensional plane strain mesoscopic model, as idealized in Fig. 1(b), considers three different domains of analysis: (i) the concrete matrix, (ii) the steel reinforcement bars and (iii) the steel–concrete interface. Each of them are characterized by a different constitutive response and FE technology that takes into account the main mechanisms involved in the corrosion process.

2.1. The concrete model

The model adopted for analyzing the concrete matrix constitutive response is an isotropic continuum damage model regularized by means of the Continuum Strong Discontinuity Approach (CSDA), as described in Oliver et al. (2002). It has been shown that this technique is robust enough and flexible to simulate different patterns of distributed cracks in solids, similar to that observed in RC structures undergoing advanced deterioration stages. Here we only summarize the main features of this model. Additional theoretical details can be obtained elsewhere (Oliver and Huespe, 2004a,b).

- (i) The macroscopic discontinuities arising in a solid, such as cracks or fractures, are mathematically described by a strong discontinuity kinematics.
  Let Ω be a given body experiencing a strong discontinuity (displacement jumps) across the surface S with normal $\boldsymbol{n}$. The surface S divides the body in two disjunct domains Ω^+ and Ω^-. The displacement $\boldsymbol{u}(\boldsymbol{x})$ and the compatible strain field $\boldsymbol{\varepsilon}(\boldsymbol{x})$, in Ω, can be written as:

$$\boldsymbol{u}(\boldsymbol{x}) = \overbrace{\bar{\boldsymbol{u}}(\boldsymbol{x})}^{\text{continuous}} + \overbrace{H_S(\boldsymbol{x})[\![\boldsymbol{u}]\!](\boldsymbol{x})}^{\text{discontinuous}}; \quad H_S(\boldsymbol{x}) = \begin{cases} 1 & \forall \boldsymbol{x} \in \Omega^+ \\ 0 & \forall \boldsymbol{x} \in \Omega^- \end{cases} \tag{1}$$

$$\boldsymbol{\varepsilon}(\boldsymbol{x}) = \nabla^{sym}\boldsymbol{u}(\boldsymbol{x}) = \underbrace{\bar{\boldsymbol{\varepsilon}}(\boldsymbol{x})}_{\text{regular}} + \underbrace{\delta_S(\boldsymbol{x})([\![\boldsymbol{u}]\!] \otimes \boldsymbol{n})^{\text{sym}}}_{\text{singular}} \tag{2}$$

where $\bar{\boldsymbol{u}}(\boldsymbol{x})$ is a continuous function in Ω, $[\![\boldsymbol{u}]\!](\boldsymbol{x})$ represents the displacement jump across the discontinuity S and $H_S(\boldsymbol{x})$ is the

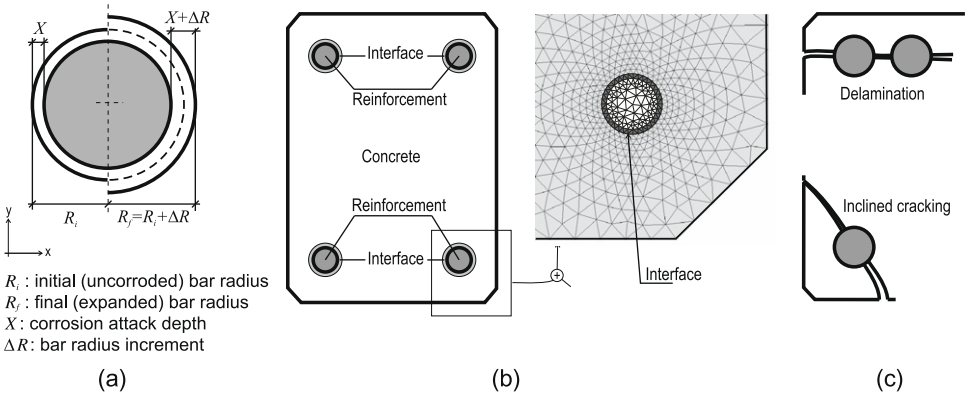

Fig. 1. RC structural member cross section. Plane strain mesoscopic 2D model: (a) Corrosion–expansion mechanism. (b) Numerical model idealization. (c) Typical pattern of cracks.

Table 1
Continuum damage model for the concrete response simulation.

Elastic stress–strain relationship

$$\boldsymbol{\sigma} = \frac{q(r)}{r}\mathbf{C}^e : \boldsymbol{\varepsilon} = [1 - d(r)]\overbrace{\mathbf{C}^e : \boldsymbol{\varepsilon}}^{\bar{\boldsymbol{\sigma}}}; \quad \mathbf{C}^e = \lambda(1 \otimes 1) + 2\mu\mathbb{I} \tag{3}$$

Damage criterion

$$\phi(\boldsymbol{\sigma}, q) = \tau_{\sigma} - q \leqslant 0 \tag{4}$$

$$\tau_{\sigma} = \chi\sqrt{\boldsymbol{\sigma} : (\mathbf{C}^e)^{-1} : \boldsymbol{\sigma}} = \chi[1 - d(r)]\sqrt{\bar{\boldsymbol{\sigma}} : (\mathbf{C}^e)^{-1} : \bar{\boldsymbol{\sigma}}} \tag{5}$$

$$\chi = \frac{\sum_{i=1}^{i=3}\langle\bar{\sigma}_i\rangle}{\sum_{i=1}^{i=3}|\bar{\sigma}_i|}\left[1 - \frac{1}{n_{\sigma}}\right] + \frac{1}{n_{\sigma}}; \quad n_{\sigma} = \frac{f_c}{f_t}; \quad \langle\bullet\rangle = \frac{1}{2}\{\bullet + \|\bullet\|\} \tag{6}$$

$\bar{\sigma}_i \equiv$ principal values of $\bar{\boldsymbol{\sigma}}$

Softening evolution law

$$\dot{r} = \gamma; \quad r_0 = r|_{t=0} = \frac{f_t}{\sqrt{E}}; \quad (\gamma \equiv \text{consistency parameter}) \tag{7}$$

$$\dot{q} = H(r)\dot{r}; \quad q_0 = q|_{t=0} = r_0; (\mathrm{H} : \text{softening modulus}) \tag{8}$$

Loading–unloading complementarity conditions

$$\phi(\boldsymbol{\sigma}, q) \leqslant 0; \quad \gamma \geqslant 0; \quad \gamma\phi(\boldsymbol{\sigma}, q) = 0 \tag{9}$$

Heaviside's step function. The strain field shows a singular term, the second one in Eq. (2), given by the Dirac's delta distribution $\delta_S(\boldsymbol{x})$.

- (ii) Concrete can be quite appropriately modeled by means of an isotropic continuum damage model equipped with a regularized strain softening response in order to make possible the onset of material instabilities, strain localization and crack propagation. Table 1 defines this material model, where damage in tension and compression is possible, but different ultimate limit stresses are used (Oliver et al., 1990). There, $\boldsymbol{\sigma}$ and $\boldsymbol{\varepsilon}$ represent the stress and strain tensors, q and r are internal variables defining the standard damage variable $d = 1 - \frac{q}{r}$, the elastic material parameters E, λ and μ are the Young's modulus and the Lamé's coefficients. Also we define f_c and f_t as the compressive and tensile limit strengths, respectively. Concrete models which considers a more ductile response in compression (Grassl and Jirásek, 2006; Cervenka and Papanikolaou, 2008; Rabczuk et al., 2005) could also be adopted without substantial changes in the present computational model.
  The compatibility between the strong discontinuity kinematics, Eqs. (1) and (2), and the continuum damage material model is performed by introducing an intrinsic softening modulus $\overline{H} = \delta_S H$, whose value is computed from the classical parameters used in the Fracture Mechanics context: $\overline{H} = f(f_t, G_f, E)$, where G_f is the concrete fracture energy. This intrinsic modulus allows one to define a bounded stress state in S through the standard continuum damage model of Table 1, even when the strains $\boldsymbol{\varepsilon}$ are defined by a singular term, see Eq. (2).
- (iii) The vector traction continuity across the discontinuity interface S, equilibrium condition, requires that:

$$\boldsymbol{t}_S = \boldsymbol{\sigma}_S \cdot \boldsymbol{n} = \boldsymbol{\sigma}_{\Omega^+} \cdot \boldsymbol{n} \tag{10}$$

When the strong discontinuity kinematics, Eqs. (1) and (2), is consistently introduced in this continuum setting, a cohesive model $\boldsymbol{t}_S = f(\llbracket\boldsymbol{u}\rrbracket)$ is automatically projected onto the interface S (Oliver, 2000). This traction–separation cohesive law governs the crack opening evolution in the strong discontinuity regime.

- (iv) The previously discussed model is numerically implemented by using a finite element technique based on embedded strong discontinuities. Basically, this methodology consists of enriching the standard continuous displacement field with enhanced discontinuous modes and, consequently, additional degrees of freedom. This technique makes possible to capture a crack intersecting a finite element in an arbitrary direction. In particular, the E-FEM technology (Oliver et al., 2006) has been adopted in the present work.

Summarizing, the non-linear analysis of the concrete response is performed with a continuum format by using standard stress–strain constitutive descriptions such as that presented in Table 1.

2.2. The steel bar model

A standard linear elastic (isotropic) constitutive relation is assumed for the steel bars. The expansion effect, due to the corrosion phenomenon, is considered through a (pseudo) volumetric initial deformation mode $\boldsymbol{\varepsilon}^0$.

Let us assume that the cross section of a typical RC member is contained in the $x - y$ plane, see Fig. 1. Making use of the standard Voigt's notation for tensors and assuming a plane strain state, the total strains can be expressed as the superposition of two terms:

$$\boldsymbol{\varepsilon} = \nabla^{sym}\boldsymbol{u}(\boldsymbol{x}) = \begin{bmatrix}\varepsilon_{xx}\\ \varepsilon_{yy}\\ \gamma_{xy}\\ \varepsilon_{zz}\end{bmatrix} = \begin{bmatrix}\varepsilon_{xx}\\ \varepsilon_{yy}\\ \gamma_{xy}\\ 0\end{bmatrix} = \overbrace{\begin{bmatrix}\frac{1}{E}(\sigma_{xx} - \nu\sigma_{yy} - \nu\sigma_{zz})\\ \frac{1}{E}(\sigma_{yy} - \nu\sigma_{zz} - \nu\sigma_{xx})\\ 2\left(\frac{1+\nu}{E}\right)\sigma_{xy}\\ \frac{1}{E}(\sigma_{zz} - \nu\sigma_{xx} - \nu\sigma_{yy})\end{bmatrix}}^{\boldsymbol{\varepsilon}^e} + \overbrace{\begin{bmatrix}\mathscr{D}\\ \mathscr{D}\\ 0\\ 0\end{bmatrix}}^{\boldsymbol{\varepsilon}^0} \tag{11}$$

where $\mathscr{D}$ is the value of the dilatational component due to the corrosion products and $\boldsymbol{\varepsilon}^e$ the elastic part, related with stresses through the classical linear elastic model $\boldsymbol{\sigma} = \mathbf{C}^e : \boldsymbol{\varepsilon}^e$. Note that the dilatational coefficient is not included in the zz component of $\boldsymbol{\varepsilon}^0$ because does not exist any expansion effect in the axial direction of the bars.

The increment of the bar radius, from the initial value R_i to the (corroded) final one $R_f(\Delta R = (R_f - R_i))$, see Fig. 1(a), depends on the corrosion attack depth X, which is an experimentally determined value. Therefore, $R_f = \hat{R}_f(X)$ and the dilatation parameter $\mathscr{D}$ can be estimated as a function of X:

$$\mathscr{D} \approx \frac{\hat{R}_f^2(X) - R_i^2}{2R_i^2} \tag{12}$$

Note that, in view of Eq. (12), the depth of corrosion attack (X) is a fundamental input data of the present model.

During the numerical simulation process, the total magnitude of dilatation $\mathscr{D}$ is applied incrementally, i.e. if nt times steps are required to perform the complete non-linear analysis, a (pseudo) volumetric expansion state $\Delta\boldsymbol{\varepsilon}^0 = \frac{\mathscr{D}}{nt}[1 \quad 1 \quad 0 \quad 0]^T$ is applied per time step, on each steel element.

2.3. The steel–concrete interface model (contact element)

A phenomenological observation of the mechanisms taking place in the steel–concrete interface, suggests that there exists a limit value for the shear stress transference (maximum bond stress τ_{max}) that depends on several factors: bar diameter, bar surface texture, confinement effects, corrosion level, etc. Eventually, when high expansion values in the steel are reached, the separation between both materials (steel and concrete) must be expected.

These effects have important consequences in the concrete fracture pattern prediction, what motivates the introduction of contact finite elements in order to simulate appropriately the steel–concrete interface, as shown in Fig. 2(a). The contact linear triangular element adopted in the present model, to simulate the interface steel–concrete interaction, has been taken from (Oliver et al.,

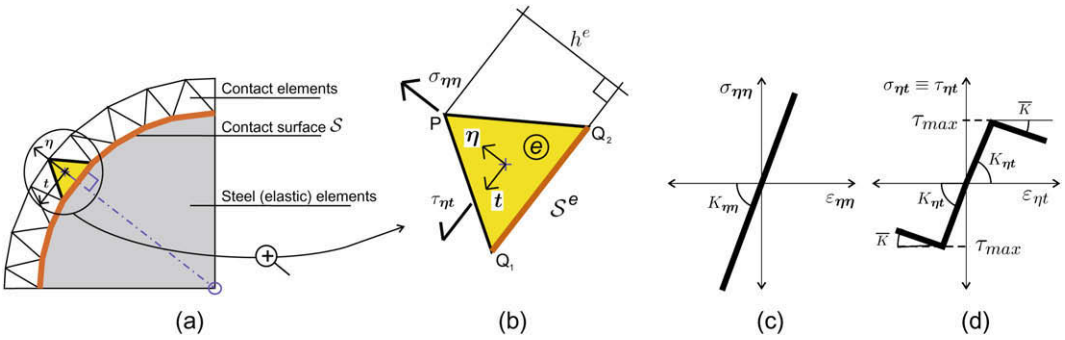

Fig. 2. Contact finite element at the interface: (a) Representative scheme. (b) Typical contact element. (c) Constitutive relation for the contact normal stress $\sigma_{\eta\eta}$. (d) Constitutive relation for the friction shear stress $\tau_{\eta t}$.

2008), where additional details about its formulation can be obtained.

In every contact finite element, it is defined a local cartesian system $\{\boldsymbol{\eta}, \boldsymbol{t}\}$, where $\boldsymbol{\eta}$ is the unit vector normal to the contact surface. The strains are evaluated from the nodal displacement, as it is done in standard finite elements. The mechanical response of the contact-friction model is expressed by means of the following constitutive law:

$$\boldsymbol{\sigma} = \Psi(g)\left[\overbrace{\sigma_{\eta\eta}(\varepsilon_{\eta\eta})(\boldsymbol{\eta}\otimes\boldsymbol{\eta})}^{\text{linear-elastic}} + \overbrace{\tau_{\eta t}(\varepsilon_{\eta t})[(\boldsymbol{\eta}\otimes\boldsymbol{t})+(\boldsymbol{t}\otimes\boldsymbol{\eta})]}^{\text{elasto-plastic}}\right];$$
$$\Psi(g) = \begin{cases} 1; & \text{if } g < 0 \\ 0; & \text{if } g \geqslant 0 \end{cases} \tag{13}$$

where the gap function, $g(\varepsilon_{\eta\eta})$, is computed as:

$$g(\varepsilon_{\eta\eta}) = h^e \varepsilon_{\eta\eta} \tag{14}$$

where h^e, is the size of the contact finite element in the $\boldsymbol{\eta}$ direction, which has not any numerical implication, and thus, it can be arbitrarily small.

The normal contact stress, $\sigma_{\eta\eta}$, is obtained as a function of the constant strain component $\varepsilon_{\eta\eta}(\varepsilon_{\eta\eta} = \boldsymbol{\eta}\cdot\boldsymbol{\varepsilon}\cdot\boldsymbol{\eta})$, following a 1D linear elastic law (see Fig. 2(c)). The friction stress component, $\tau_{\eta t}$, is determined as a function of the constant shear strain component $\varepsilon_{\eta t}(\varepsilon_{\eta t} = \boldsymbol{\eta}\cdot\boldsymbol{\varepsilon}\cdot\boldsymbol{t})$ by means of a classical 1D elasto-plastic constitutive model, as detailed in Table 2 (see also Fig. 2(d)). The elasto-plastic model of Table 2 only applies when $\Psi(g) = 1$, otherwise no evolution of plastic flow is considered.

Table 2
Basic equations for the 1D elasto-plastic frictional model ($\tau_{\eta t}$ shear stress).

Incremental elastic stress–strain relationship

$$\dot{\tau}_{\eta t} = K_{\eta t}(\dot{\varepsilon}_{\eta t} - \dot{\varepsilon}^p_{\eta t}) \tag{15}$$

Yield condition

$$\phi(\tau_{\eta t}, \alpha) = |\tau_{\eta t}| - (\tau_{max} + \overline{K}\alpha) \leqslant 0 \tag{16}$$

Flow rule and hardening/softening evolution law

$$\dot{\varepsilon}^p_{\eta t} = \gamma\,\text{sign}(\tau_{\eta t}); \quad (\gamma \equiv \text{plastic multiplier}) \tag{17}$$
$$\dot{\alpha} = \gamma; \quad (\alpha \equiv \text{accumulated equivalent plastic strain}) \tag{18}$$

Loading–unloading complementarity conditions

$$\phi(\tau_{\eta t}, \alpha) \leqslant 0; \quad \gamma \geqslant 0; \quad \gamma\phi(\tau_{\eta t}, \alpha) = 0 \tag{19}$$

Summarizing, the proposed contact-friction model is characterized by four parameters: the normal stiffness ($K_{\eta\eta}$) working as a penalty parameter, the shear stiffness ($K_{\eta t}$), the maximum bond stress (τ_{max}) and the hardening/softening shear modulus ($\overline{K}$).

3. Mesoscopic model to simulate the structural load carrying capacity

The model of Section 2 provides qualitative information related to the concrete degradation mechanisms due to the steel expansion. Nevertheless, it does not give additional information about the mechanical behavior of a deteriorated RC structure subjected to external loads.

In this, Section we introduce a 2D mesoscopic model for the quantitative prediction of the residual load carrying capacity of corroded RC members, where each component of the structure (concrete, steel and steel–concrete interface) is independently represented. The model is applied to a longitudinal section of the member in plane stress state. An idealized scheme of the adopted discrete model, applied to an RC beam, can be observed in Fig. 3.

The present (plane stress) mesoscopic strategy has many similar features with the (plane strain) mesoscopic model of the previous Section 2. In fact, the concrete model we adopt here follows the CSDA methodology discussed in sub-Section 2.1, with identical enhanced finite elements technology, isotropic (tension–compression) continuum constitutive damage model and crack propagation scheme. Furthermore, a similar procedure to that described in sub-Section 2.3 is here adopted for the steel–concrete interface model. Note that, in the present case, the contact elements provide the necessary mechanical coupling between the concrete matrix and the reinforcements acting as top/bottom longitudinal bars and stirrups. Consequently, a consistent definition of the unit normal vector, $\boldsymbol{\eta}$, is required in each contact finite element.

The mechanical behavior of the steel bars is simulated with an elasto-plastic model, which is briefly discussed in the following sub-Section.

3.1. Elasto-plastic model for the longitudinal steel reinforcement bars

The steel bar response is characterized by a 2D finite element model. Each finite element has associated a local normalized cartesian basis $\{\boldsymbol{\eta}, \boldsymbol{t}\}$. The vector $\boldsymbol{\eta}$ is computed such that it is orthogonal to the longitudinal bar axis, see Fig. 4(a). The reinforcement mechanical behavior reproduces a 1D standard elasto-plastic model in the σ_{tt} normal stress component, while the remaining stress tensor components behave elastically, assuming a Poisson ratio $\nu = 0$.

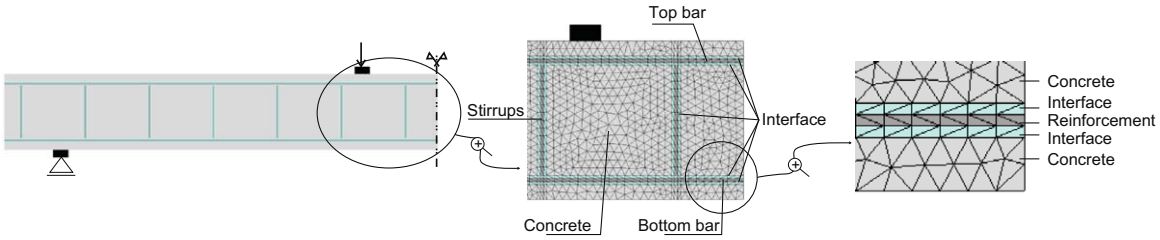

Fig. 3. Plane stress mesoscopic 2D model for the longitudinal section of the beam.

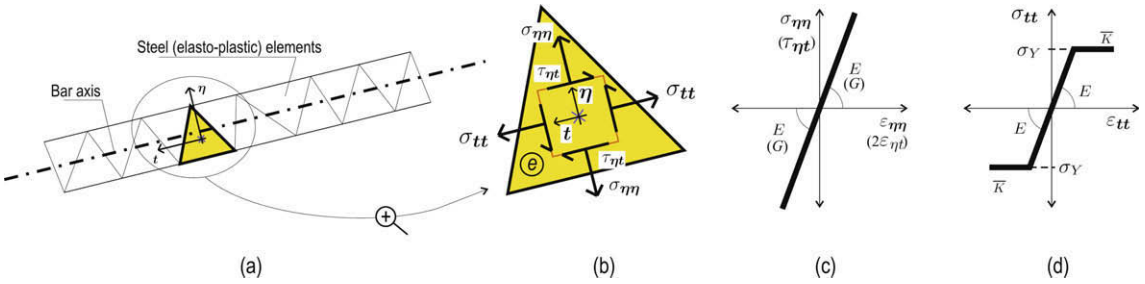

Fig. 4. Elasto-plastic reinforcement element: (a) Representative scheme. (b) Typical steel element. (c) Constitutive relation for $\sigma_{\eta\eta}$ and $\tau_{\eta t}$ stresses. (d) Constitutive relation for σ_{tt} stress.

Thus, the stress tensor is given by:

$$\boldsymbol{\sigma} = \underbrace{\sigma_{\eta\eta}(\boldsymbol{\eta}\otimes\boldsymbol{\eta}) + \tau_{\eta t}[(\boldsymbol{\eta}\otimes\boldsymbol{t}) + (\boldsymbol{t}\otimes\boldsymbol{\eta})]}_{\text{linear-elastic}} + \underbrace{\sigma_{tt}(\boldsymbol{t}\otimes\boldsymbol{t})}_{\text{elasto-plastic}} \tag{20}$$

where $\sigma_{\eta\eta} = E\varepsilon_{\eta\eta}$, $\tau_{\eta t} = \tau_{t\eta} = G2\varepsilon_{\eta t}$ ($G = \frac{E}{2}$ being the shear modulus), see Fig. 4(c), and σ_{tt} is given by a standard 1D plasticity model characterized by three parameters: the Young's modulus (E), the uniaxial yield stress (σ_Y) and the hardening/softening modulus ($\overline{K}$).

4. Coupling strategy between the cross section and the structural member model

Fig. 5 shows an idealized scheme of the strategy adopted in this work to couple the two models presented in the previous Sections, i.e. the cross section analysis and the structural member (longitudinal section) analysis.

As it can be observed in the figure we transfer, from one domain of analysis (the geometric cross section) to the structural member domain, the average value of the damage variable "d" across horizontal slices in the cross section geometry. This projection is consistent because both analysis use the same continuum isotropic damage model for simulating the concrete domain. Thus, the final concrete degradation state induced by the steel bar volumetric deformation process, is considered to be the initial damage condition for the subsequent structural analysis. This means that we are assuming that the two mesoscopic models are coupled in only one direction, neglecting the structural load effects on the concrete damage evaluation determined in the cross section analysis. A complete coupling between these mechanisms could be obtained by using a 3D model with identical ingredients to that presented in the preceding Section.

Note that, in the present strategy, neither ad-hoc assumptions about reductions in the net cross section area of the concrete nor empirical modifications in the definition of its constitutive behavior are introduced in order to simulate the degradation by corrosion in the concrete matrix, in contrast with other simpler models previously proposed in the literature for corroded RC members. This complex phenomenon is taken into account in a unique constitutive scenario (continuum damage model) performing a consistent mapping of the damage variable between the two level of analysis.

5. Numerical results

In this Section, a series of numerical simulations is addressed in order to test the performance of the described finite element formulations. Three types of RC beams have been analyzed, as in the original reference (Rodriguez et al., 1995) we call them: beam type 11, 31 and 13 (additional indices will be added to indicate different corrosion levels). The geometry and boundary conditions of the examples are shown in Fig. 6. Table 3 presents additional information on the geometry and material data. The differences between the beam types are the reinforcement arrangements (steel ratios of top/bottom bars and stirrups separations).

For these specimens, experimental results are available, see Rodriguez et al. (1995, 1996). In these works a process of accelerated corrosion was induced by applying a constant anodic current density of 100 [μA/cm^2] in the embedded steel bars and also by using a contaminated concrete mixture with calcium chloride, which produces a generalized corrosion phenomenon. Table 4 shows some experimental measurements of the attack depth X, for different levels of corrosion and types of reinforcement.

Previously, Coronelli and Gambarova (2004) have presented a numerical mesoscopic 2D model for corroded RC elements, which has been validated with the set of beams 11 and 31 of Rodriguez et al. (1995). In particular, all these beams (11 and 31) have failed due to bending failure modes.

In the present work, and following very closely the guidelines and material characterization reported in Coronelli and Gambarova (2004), we show the capacity of the present model to capture the typical bending failure modes and limit load computations, as also, the coupled mechanisms of shear combined with anchorage failure of tensile bars (bond failure). Results, for all cases, are compared with the reported experimental information.

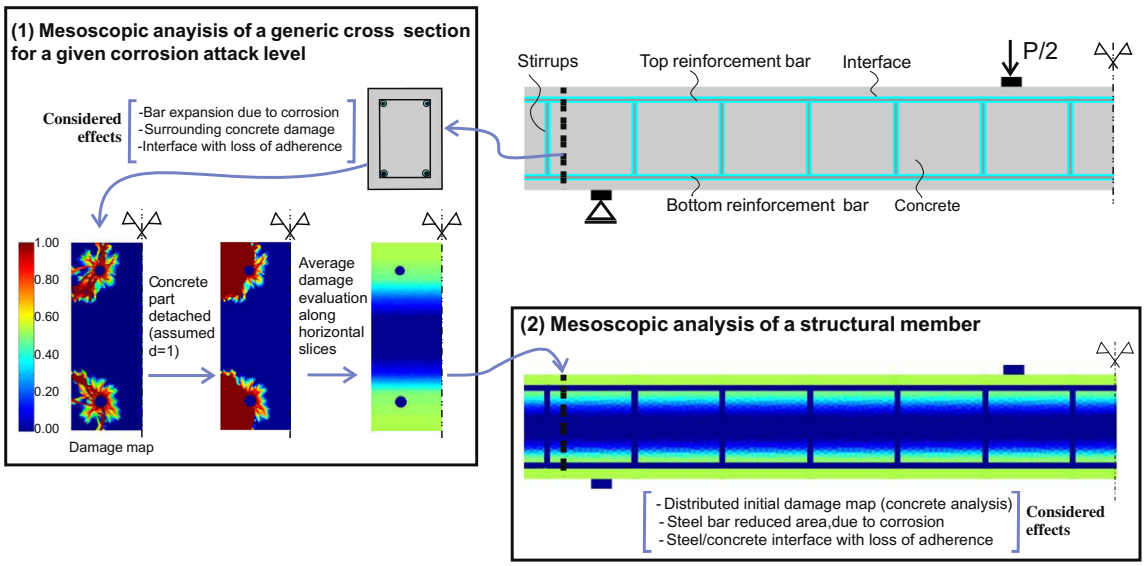

Fig. 5. Coupling strategy between the cross section analysis and the structural member analysis.

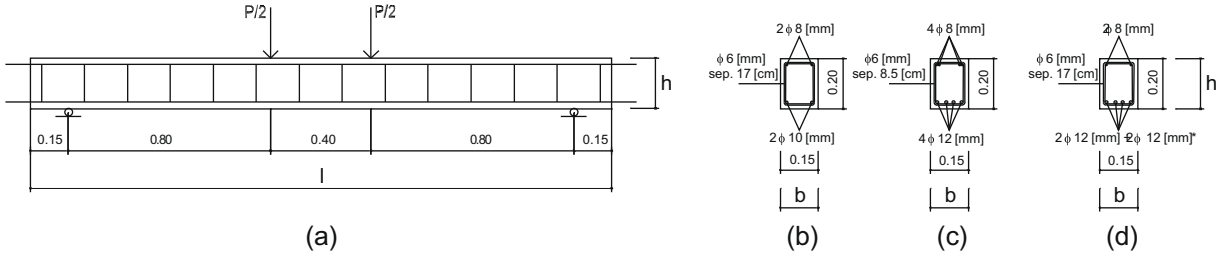

Fig. 6. RC beams: (a) Dimensions and boundary conditions (length in [m], except the specified ones). (b) Cross section diagram for beam type 11, $\approx 0.5\%$ steel–concrete ratio. (c) Cross section diagram for beam type 31, $\approx 1.5\%$ steel–concrete ratio. (d) Cross section diagram for beam type 13, $\approx 1.5\%$ steel–concrete ratio (2 ∅ 12 [mm]* cut-off bars outside of the support zone).

Table 3
RC beams. Material description, taken from Coronelli and Gambarova (2004) and Rodriguez et al. (1995) (2 ∅ 12 [mm]* cut-off bars).

(1) Beam type	(2) Dimensions $l \times b \times h$ [m]	(3) Top bars number/ diameter [mm]	(4) Bottom bars number/ diameter [mm]	(5) Stirrups diameter/ spacing [mm]	(6) Concrete strength: f_c [MPa]	(7) Steel yield stress: σ_Y [MPa]
11	$2.00 \times 0.15 \times 0.20$	2 ∅ 8	2 ∅ 10	∅6/170	50–34	575
31	$2.00 \times 0.15 \times 0.20$	4 ∅ 8	4 ∅ 12	∅6/85	49–37	575
13	$2.00 \times 0.15 \times 0.20$	2 ∅ 8	2 ∅ 12 + 2 ∅ 12*	∅6/170	52–37	575

Table 4
Experimental corrosion attack measures, residual adherence stress τ_{max}, and experimental failure mechanism (taken from Coronelli and Gambarova (2004) and Rodriguez et al. (1995)).

(1) Beam denomination	(2) Bottom bars attack: X [mm]	(3) Top barsattack: X [mm]	(4) Stirrup attack: X [mm]	(5) τ_{max} [MPa]	(6) Experimental failure mode (denomination) – description
11-1	–	–	–	6.86	(I) – Bending: yielding in bottom reinforcement
11-4	0.45	0.52	0.39	4.10	(I) – Bending: yielding in bottom reinforcement
11-5	0.36	0.26	0.37	4.13	(I) – Bending: yielding in bottom reinforcement
11-6	0.70	0.48	0.66	4.04	(I) – Bending: yielding in bottom reinforcement
31-1	–	–	–	7.82	(II) – Bending: crushing in concrete
31-3	0.30	0.20	0.35	5.12	(II) – Bending: crushing in concrete
31-4	0.48	0.26	0.50	5.06	(II) – Bending: crushing in concrete
13-4	0.32	0.30	0.34	5.00	(IV) – Shear combined with anchorage bond failure

5.1. General aspects of the numerical simulations

Triangular finite elements with linear interpolation have been adopted for all the tests. In particular, enhanced strong discontinuity triangular elements are used for the concrete material. The numerical algorithm used to integrate the non-linear constitutive models has been the *Impl-Ex* method (Oliver et al., 2008).

In order to optimize the computational resources and computing effort, we have taken advantage of as many symmetry conditions as possible.

The material parameter characterization is based on the following considerations:

- The concrete compressive limit strength, f_c, is given in Table 3, column 6 (the first figure corresponds to the concrete used in the not corroded beams and the second one to the contaminated concrete mixture). The ultimate concrete tensile stress, f_t, is assumed as: $f_t = 0.10 f_c$. Other material properties adopted for the concrete are: $E = 28$ [GPa], $\nu = 0.2$, $G_f = 100$ [N/m].
- The contact model depends on the ultimate bond stress $\tau_{max}(X)$. Column 5 of Table 4 (see also Rodriguez et al. (1994)) provides a reasonable estimation for the bond-slip model, as a function of the corrosion level.
- The dilatation component $\mathscr{D}$, utilized in the mesoscopic plane strain model, is computed from Eq. (12). Following (Molina et al., 1993; Coronelli and Gambarova, 2004) we adopt the relation: $R_f = R_i + X$, which is based on the incompressibility assumption of the corrosion products. For each solved case, the X value is adopted from Table 4, columns 2–4.
- Finally, the steel yield stress (σ_Y) is reported in Table 3, column 7. The reinforcement cross section reduction, due to corrosion, is computed assuming a constant effective bar radius $R_{eff} = R_i - X$. Perfect plasticity is assumed, thus, the steel responds with infinite ductility, which implies that there is not neither limit strain nor bar rupture. Effects such as pitting corrosion which modifies the steel ductility and locally reduces the bar radius are not considered in the present simulation. Note that these characterizations apply, only, to the structural member (longitudinal section) analysis.

5.2. Numerical results: qualitative validation of the mesoscopic cross section model

In this sub-Section, we describe the numerical results obtained with the cross section model (see Section 2) produced by the expansion mechanism of steel bars for a predefined corrosion attack depth, and the degradation induced in the concrete.

Fig. 7 shows, for the beam type 11 in the final stage of analysis, the iso-displacement contour lines, the FE mesh in the (amplified) deformed configuration and the damage distribution in the cross section. At the end of analysis, the iso-displacement contour lines identify the failure mechanism. Cracks are represented by a higher displacement gradient, thus, a denser distribution of iso-lines describes the trajectory of active tensile macro cracks. Furthermore, in view of the continuum isotropic damage model of Table 1, the damage variable "d" accounts for the distribution of the concrete crack pattern produced during the complete loading process and which does not necessarily identify the final structural failure mechanism. Notice that "$d = 1$" represents a completely degraded material. In this sense, it is observed, for the applied expansion levels, a complete concrete degradation around the steel bars. Observe that the main local failure mechanism is an inclined crack pattern.

Fig. 8 shows, for the beam type 31, in the final stage of analysis, the iso-displacement contour lines, the deformed (scaled) configuration and the damage map. Similar to the beam 11 case, a

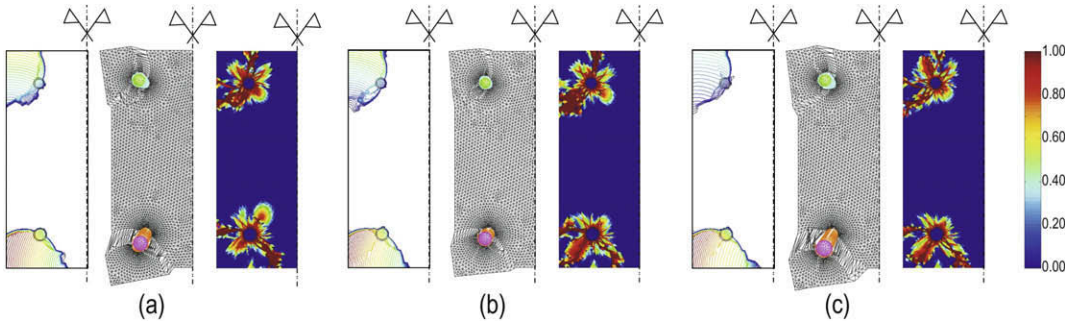

Fig. 7. Plane strain reinforcement expansion analysis. Iso-displacement contour lines (crack pattern), scaled deformed configuration and damage contour fill: (a) Beam 11-4. (b) Beam 11-5. (c) Beam 11-6.

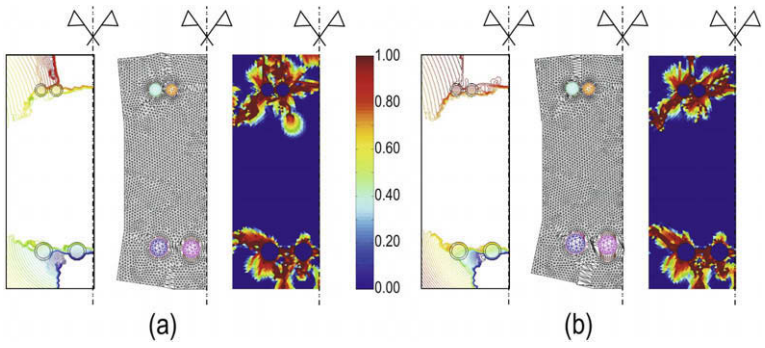

Fig. 8. Plane strain reinforcement expansion analysis. Iso-displacement contour lines (crack pattern), scaled deformed configuration and damage contour fill: (a) Beam 31-3. (b) Beam 31-4.

complete concrete degradation around the bars is observed. However, in this case, the local failure mechanism is delamination between adjacent bars and inclined cracking for the extreme steel reinforcements.

The Rodriguez's contribution (Rodriguez et al., 1995) displays the "typical pattern of longitudinal cracks", observable at the whole length of the beam type 21-4, induced by the expansion of the embedded corroded bars. In Fig. 9 we reproduce, schematically, his experimental result. Even though we have not analyzed this particular beam typology, considering Figs. 7 and 8 depicted in our contribution, they clearly demonstrate that the typical phenomenology of longitudinal cracks is effectively captured. Those fractures reaching the actual boundary of the cross section (due to the symmetry assumption along the long beam axis) should be interpreted as longitudinal cracks.

In general, at the cross section level and from a qualitative point of view, it can be observed that the proposed mesoscopic plane strain numerical model captures physically admissible failure mechanisms. The introduction of friction-contact (interface) finite elements in the simulations has been a key point in order to obtain these consistent patterns of cracks.

Also, it can be mentioned that the so obtained crack pattern matches very well with the semi-analytical predictions reported in Capozucca (1995) (which were deduced from the physical mathematical model developed by Bazant (1979a,b)):

$$\text{if } S > (6D) \rightarrow \text{inclined cracking prevails}$$

$$\text{if } L > \frac{(S-D)}{2} \rightarrow \text{delamination mechanism prevails}$$

where S is the horizontal spacing of bars, D the diameter of the reinforcement bars and L the cover depth.

Note that the cross section model can be applied for arbitrary geometries of the beam cross section and for any distribution of embedded bars. Besides, each steel bar can be subjected to a different level of corrosion, and consequently to a different expansion level. For each one of these (hypothetical) situations a complete degradation pattern can be obtained and, therefore, an initial damage distribution for the subsequent structural analysis can be estimated. Even more, the restriction to modeling generalized corrosion must be considered as an hypothesis and not as a limitation of the model. If information about different levels of localized corrosion in specific points (or zones) of the beam were available, a mesoscopic analysis could be applied for each one of these cross sections and then different initial degradation patterns could be applied to different zones at the structural level.

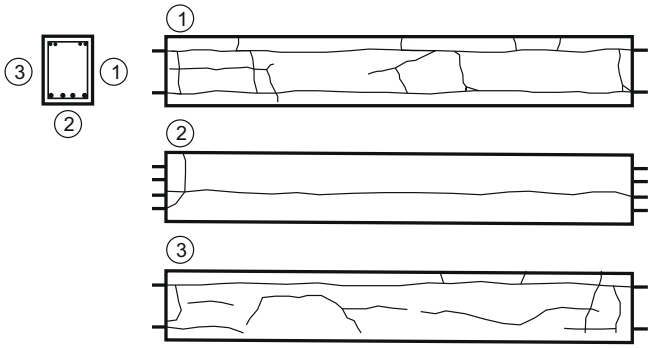

Fig. 9. Experimental pattern of longitudinal cracks obtained by Rodriguez et al. (1995). Beam type 21-4.

5.3. Numerical results: quantitative and qualitative validation of the mesoscopic structural model

The main quantitative result, determined from the previous analysis, is the distribution of the damage variable at the whole cross section. Taking into account the coupling philosophy described in Section 4, this information is post-processed in order to impose an initial degradation condition for the RC members. A subsequent structural analysis is performed using the model discussed in Section 3. Here, we show the main results of this approach, when it is applied to the beam types 11 and 31 for capturing bending failure modes.

Fig. 10 depicts the obtained damage distribution, the iso-displacement contour lines (in the z-direction), which represent the trajectory of active macro cracks at the end of the simulation, and the axial σ_{zz} stress contour fill, for two of the beams type 11

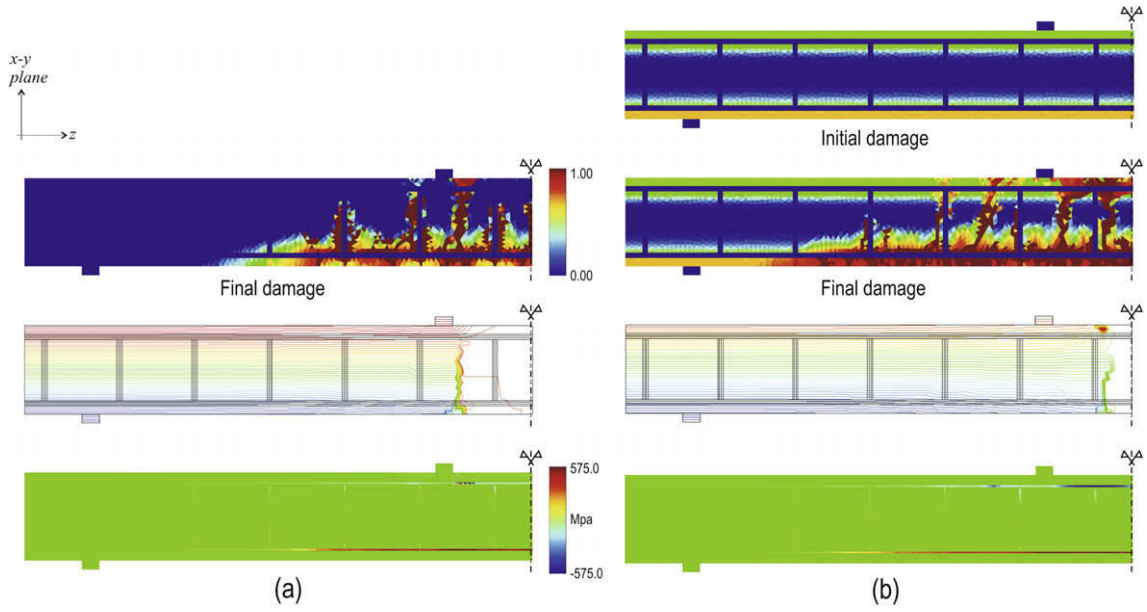

Fig. 10. Plane stress mesoscopic model. Damage contour fill, z-direction iso-displacement contour lines and σ_{zz} contour fill: (a) Beam 11-4 (not corroded case). (b) Beam 11-4 (corroded case).

(the not corroded case 11-1 and the corroded one 11-4, from Table 4). The same analysis, applied to beam type 31, provides the results displayed in Fig. 11.

Fig. 12(a) shows, schematically, the different failure mechanisms observed in the experimental program carried out by Rodriguez et al., see also Table 4. They reported four failure modes: (I) bending with yielding in bottom bars, (II) bending with concrete crushing, (III) pure shear, and (IV) shear combined with steel–concrete bond degradation. In the same Figure, we depict the concrete crushing zone and the distribution of tensile macro cracks obtained using the present numerical model for the case of the beam 11-6 and 31-4 (similar results were obtained for different corrosion attacks). Here, the crushing zone is understood as the concrete domain where damage in compression is reached. Notice that the simulations predict failure by bending. Additionally, the numerical model distinguishes between both failure mechanisms due to bending: mode I (beam type 11-6, as observed in Fig. 12(b)) and II (beam type 31-4, displayed in Fig. 12(c)). From a qualitative point of view, a good agreement between the predicted and observed bending failure mechanisms is obtained.

In Figs. 13–16 we show the evolution of the total vertical load vs. the mid span vertical displacement curves, obtained using the proposed mesoscopic model, for the beam types 11 and 31. Those curves are contrasted with experimental (Rodriguez et al. (1996)) and numerical results (Coronelli and Gambarova (2004)). A good agreement with them has been obtained. In general, we note a fairly adjustment of our numerical results, if compared with the experimental ones, than that presented by Coronelli and Gambarova (2004).

It can be seen that the typical behavior of the RC beams is appropriately captured, i.e. the existence of three well defined slopes in the mechanical response (see Figs. 13–16): an initial stiffness associated with the undamage state (without cracks) in the concrete, an intermediate stiffness characterized by the evolution

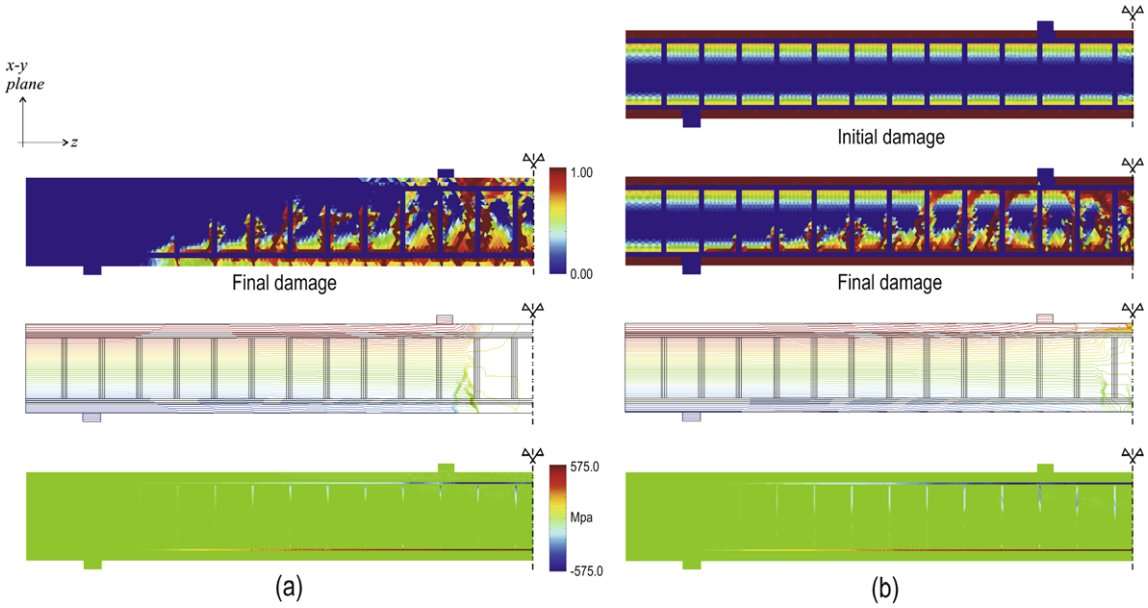

Fig. 11. Plane stress mesoscopic model. Damage contour fill, z-direction iso-displacement contour lines and σ_{zz} contour fill: (a) Beam 31-1 (not corroded case). (b) Beam 31-3 (corroded case).

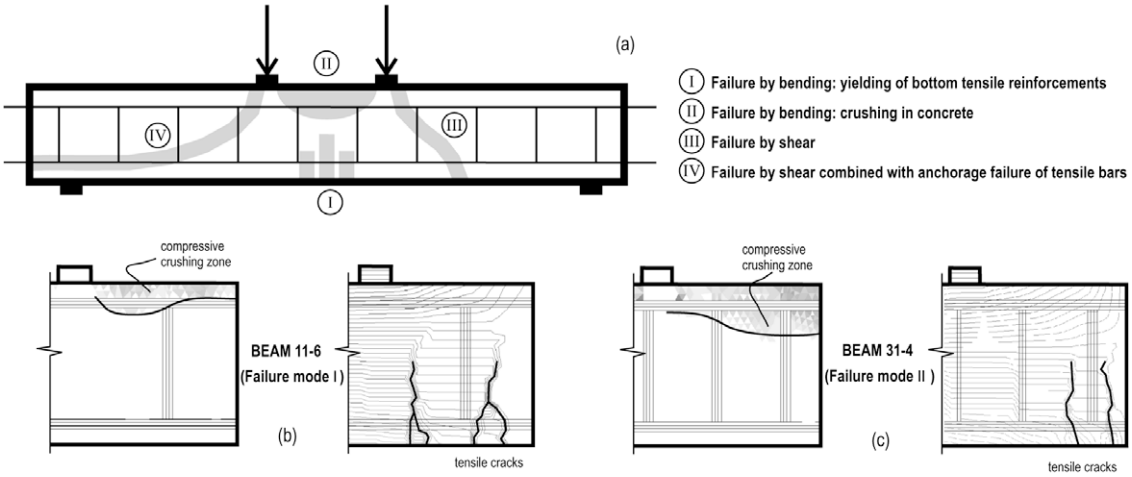

Fig. 12. Failure mechanisms for the studied beam types: (a) Experimental failure modes reported by Rodriguez et al. (1995). (b) Beam 11-6: crushing zone and distribution of tensile macro cracks. (b) Beam 31-4: crushing zone and distribution of tensile macro cracks.

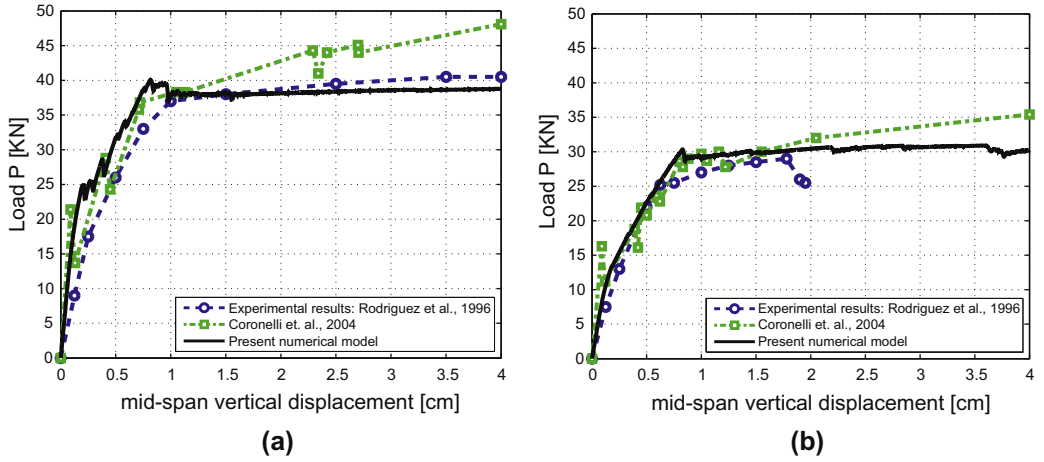

Fig. 13. Load vs. displacement structural response: (a) Beam 11-1. (b) Beam 11-4.

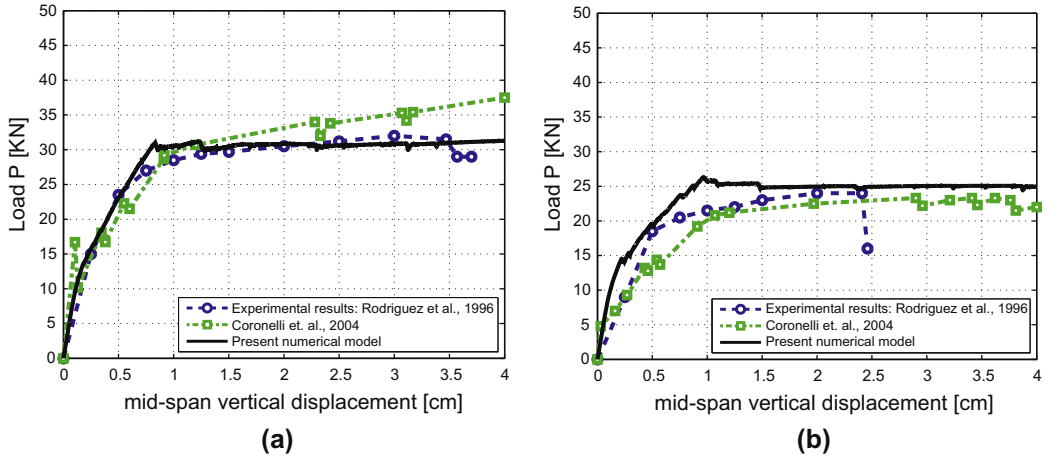

Fig. 14. Load vs. displacement structural response: (a) Beam 11-5. (b) Beam 11-6.

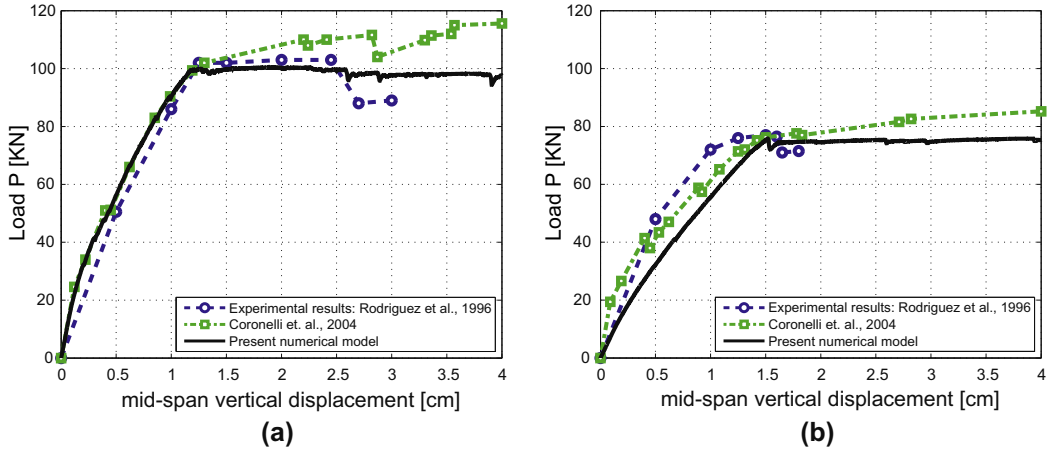

Fig. 15. Load vs. displacement structural response: (a) Beam 31-1. (b) Beam 31-3.

and propagation of multiple tensile macro-fractures in the concrete and a (pseudo-horizontal) final plateau which defines the limit mechanism of failure due to reaching either the ultimate compressive strength of concrete or yielding in the steel reinforcements. Some differences between the initial and intermediate numerical stiffness with the experimental results may be due to: (i) uncertainties in the elastic material parameter characterizations, (ii) the lack of data on the statistical deviation induced by the experimental results and (iii) the approximate estimation of the concrete degradation area, in a generic cross section, when

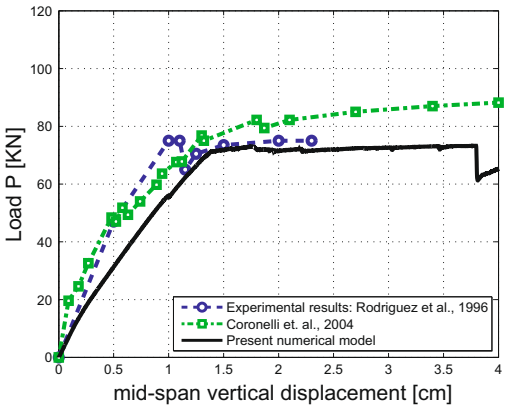

Fig. 16. Load vs. displacement structural response. Beam 31-4.

transferring the damage from the cross section analysis to the structural level analysis (it means that an essentially three dimensional phenomenon is assumed as a two dimensional one with symmetry along the larger structural axis).

5.4. Numerical results: assessment of the failure mode sensitivity with the value of the ultimate bond stress

An additional test has been carried out in order to evaluate the sensitivity of the failure mechanism with the value of the ultimate bond stress. We simulate the beam number 13-4 presented by Rodriguez et al. (1995). From the experimental observation, they reported that the beam series 13 displays a combined shear and bond failure mechanisms (mode IV in Fig. 12(a)).

The distribution and quantity of reinforcements of the experimental test is displayed in Fig. 6(a)–(d) and Table 3; notice that a 50 % of the tensile reinforcement is anchored outside of the support zone. In the same Table, the geometry of the beam is presented, as also, the concrete strength and reinforcement yield stress.

The sensitivity analysis is performed by modifying the contact model limit bond stress (τ_{max} in Fig. 2), which is directly correlated with the corrosion attack depth X. Results have been obtained with $2\tau_{max}$, τ_{max} and $0.5\tau_{max}$, where the parameter $\tau_{max} = 5.0$ [MPa], see Table 4, has been adopted from the estimations of Coronelli and Gambarova (2004), for similar degrees of reinforcement corrosion.

The load vs. displacement curves are plotted in Fig. 17(a). It is to be noted that the experimental ultimate load value (shear force: $P/2$) reported by Rodriguez et al. (1995) for this beam is 34.6 [MPa], which is in between our numerical results with τ_{max} and $2\tau_{max}$. In this figure, it is noticeable the effect that the contact model limit shear stress has on the ultimate structural load.

Fig. 17(b) displays the crack pattern distribution obtained with the numerical model. A remarkable failure mode transition from bending-shear dominant to debonding dominant mechanisms is observed by lowering the contact model limit shear stress values, which is correlated with the reinforcement corrosion attack. The present model captures partially the phenomenology associated to the shear and debonding mechanisms of failure. However, we have not captured the abrupt structural strength loss of some experimental results. A variable degree of ductility, should be also observed in some of the load vs. deflection plots of Figs. 13–16. This is a limitation of the model, which can be partially explained because we do not simulate the pitting corrosion phenomenon, which in most of the experimental cases could be the cause of premature failure.

As far as we know, there is not available a simplified evaluation of the limit load prediction (upper and lower bounds) based on limit states for the complete range of combined shear-bend-bond failure modes displayed in this test.

6. Conclusions

We have presented an application of the CSDA methodology to solve RC structural problems undergoing a reinforcement corrosion phenomenon. As a novel contribution, two different mesoscopic size-scale models have been developed: at the cross section level and at the global or structural level. A coupling strategy between them has also been presented.

Contact finite elements were considered in these formulations in order to improve the simulation of the steel–concrete interface effects. Following the proposed methodology, the most relevant corrosion mechanisms can be simulated, for example: expansion of steel bars, damage/cracking in the concrete, yielding in the reinforcements, bond stress degradation at the interface and steel cross section reduction.

The model provides information in all the degradation process stages (continuous evaluation of the structural strength deterioration). Therefore, it could be used to compute limit states, as also, to predict possible mechanisms that affect the structural *serviceability* for an hypothetical level of corrosion. In summary, it represents a viable technique to analyze deteriorated RC members.

Additional conclusions that can be obtained from the numerical simulations are:

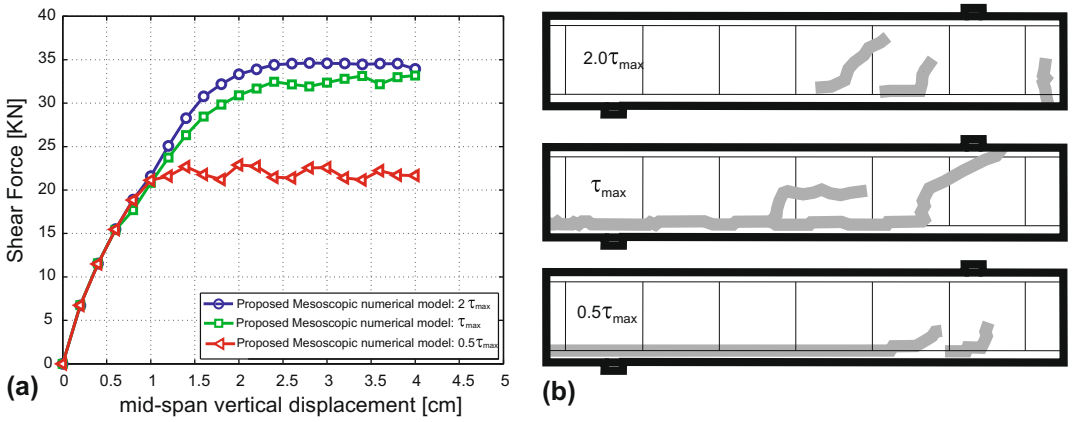

Fig. 17. Assessment of the failure mode sensitivity with the ultimate bond stress: (a) Load vs. displacement structural responses. (b) Failure mode detected with three different bond strength ($\tau_{max} = 5$ [MPa]).

- The mesoscopic plane strain model of the cross section captures adequately the experimental crack patterns. Inclined cracking or delamination modes have been obtained, depending on the location and separation of reinforcement bars. The proposed model can be applied to more sophisticated RC cross section geometrical designs to obtain a qualitative idea of the deterioration mechanisms induced by the expansion–corrosion process.
- At the structural level, the mesoscopic plane stress model of the longitudinal section captures physically admissible concrete degradation patterns and also, partially, the transition between different failure mechanisms. The sensitivity of the limit load evaluations with the reinforcement corrosion level has been acceptably computed.

In contrast to previous models proposed in the literature for analyzing corroded RC members, in the present strategy, we do not adopt any ad-hoc assumptions about the concrete net cross-section area reduction neither empirical modifications in the definition of the concrete matrix constitutive relation in order to simulate the degradation process induced by the reinforcement corrosion. It comes out from the mesoscopic cross sectional analysis and is one of the key aspect of the proposed methodology.

Future developments will be devoted to consider the pitting effect as also the inclusion of an adequate failure criterion for the steel reinforcements (both bars and stirrups) in order to improve the prediction capability of the present model, specially for capturing transition from ductile to quasi-brittle failure modes.

Acknowledgments

Financial support from the Spanish Ministry of Science and Technology through grant BIA-2008-00411 and from ANPCyT of Argentina through grants PICT-2005- 34273 and PICT-2006-1232, are gratefully acknowledged.

References

Almusallam, A.A., Al-Gahtani, A.S., Aziz, A.R., Rasheeduzzafar, 1996. Effect of reinforcement corrosion on bond strength. Constr. Build. Mater. 10 (2), 123–129.

Al-Sulaimani, G.J., Kaleemullah, M., Basumbul, I.A., Rasheeduzzafar, 1990. Influence of corrosion and cracking on bond behavior and strength of reinforced concrete members. ACI Struct. J. 87 (2), 220–231.

Bazant, Z.P., 1979a. Physical model for steel corrosion in concrete sea structures – theory. J. Struct. Div., 1137–1153.

Bazant, Z.P., 1979b. Physical model for steel corrosion in concrete sea structures – applications. J. Struct. Div., 1155–1165.

Bhargava, K., Ghosh, A.K., Mori, Y., Ramanujam, S., 2006. Model for cover cracking due to rebar corrosion in rc structures. Eng. Struct. 28, 1093–1109.

Bhargava, K., Ghosh, A.K., Mori, Y., Ramanujam, S., 2007. Corrosion-induced bond strength degradation in reinforced concrete – analytical and empirical models. Nucl. Eng. Des. 237, 1140–1157.

Cabrera, J.G., Ghoddoussi, P., 1992. The effect of reinforcement corrosion on the strength of the steel/concrete bond. In: Proc. Int. Conf. on Bond in Concrete. Riga, Latvia, CEB, pp. 10/11–10/24 .

Capozucca, R., 1995. Damage to reinforced concrete due to reinforcement corrosion. Constr. Build. Mater. 9 (5), 295–303.

Castellani, A., Coronelli, D., 1999. Section 13.7: beams with corroded reinforcement: evaluation of effects of cross section losses and bond deterioration by finite element analysis. In: Forde, M. (Ed.), Proc. 8th Int. Conf. on Structure Faults and Repair. Engineering Tech. Press, Edinburgh, UK. 99p (CD-ROM)..

Cervenka, J., Papanikolaou, V.K., 2008. Three dimensional combined fracture-plastic material model for concrete. Int. J. Plast. 24, 2192–2220.

Coronelli, D., Gambarova, P., 2004. Structural assessment of corroded reinforced concrete beams: modeling guidelines. J. Struct. Eng. ASCE 130 (8), 1214–1224.

Fang, C., Lundgren, K., Plos, M., Gylltoft, K., 2006. Bond behaviour of corroded reinforcing steel bars in concrete. Cem. Concr. Res. 36, 1931–1938.

Grassl, P., Jirásek, M., 2006. Damage-plastic model for concrete failure. Int. J. Solids Struct. 43, 7166–7196.

Huang, R., Yang, C.C., 1997. Condition assessment of reinforced concrete beams relative to reinforcement corrosion. Cem. Concr. Compos. 19, 131–137.

Molina, F.J., Alonso, C., Andrade, C., 1993. Cover cracking as a function of rebar corrosion. II: numerical model. Mater. Struct. 26, 532–548.

Okada, K., Kobayashi, K., Miyagawa, T., 1988. Influence of longitudinal cracking due to reinforcement corrosion on characteristics of reinforced concrete members. ACI Struct. J. 85 (2), 134–140.

Oliver, J., 2000. On the discrete constitutive models induced by strong discontinuity kinematics and continuum constitutive equations. Int. J. Solids Struct. 37, 7207–7229.

Oliver, J., Huespe, A.E., 2004a. Theoretical and computational issues in modelling material failure in strong discontinuity scenarios. Comput. Meth. Appl. Mech. Eng. 193, 2987–3014.

Oliver, J., Huespe, A.E., 2004b. Continuum approach to material failure in strong discontinuity settings. Comp. Meth. Appl. Mech. Eng. 193, 3195–3220.

Oliver, J., Cervera, M., Oller, S., Lubliner, J., 1990. Isotropic damage models and smeared crack analysis of concrete. In: Bicanic, N., et al. (Eds.), SCI-C Computer Aided Analysis and Design of Concrete Structures. Pineridge Press, Swansea, pp. 945–957.

Oliver, J., Huespe, A.E., Pulido, M.D.G., Chaves, E., 2002. From continuum mechanics to fracture mechanics: the strong discontinuity approach. Eng. Fract. Mech. 69, 113–136.

Oliver, J., Huespe, A.E., Sánchez, P.J., 2006. A comparative study on finite elements for capturing strong discontinuities: e-fem vs x-fem. Comput. Methods Appl. Mech. Eng. 195 (37–40), 4732–4752.

Oliver, J., Huespe, A.E., Cante, J., 2008. An implicit/explicit integration scheme to increase computability of non-linear material and contact/friction problems. Comp. Meth. Appl. Mech. Eng. 197 (21–24), 1865–1889.

Rabczuk, T., Akkermann, J., Eibl, J., 2005. A numerical model for reinforced concrete structures. Int. J. Solids Struct. 42, 1327–1354.

Rodriguez, J., Ortega, L., Garcia, A., 1994. Corrosion of reinforcing bars and service life of r/c structures: corrosion and bond deterioration. In: Proc. Int. Conf. on Concrete Across Borders, vol. 2. dense, Denmark, .

Rodriguez, J., Ortega, L., Casal, J., 1995. Load carrying capacity of concrete structures with corroded reinforcement. In: Forde, M. (Ed.), 4th Int. Conf. on Structure Faults and Repair. Engineering Tech. Press, Edinburgh, UK, pp. 189–199.

Rodriguez, J., Ortega, M., Casal, J., Diez, M.D., 1996. Assesing structural conditions of concrete structures with corroded reinforcement. In: Dhir Dundee, R.K., Henderson, N.A. (Eds.), Proc. Int. Conf. on Concrete in the Service of Mankind. E&FN Spon, London, pp. 141–150.

Tachibana, Y., Maeda, K.I., Kajakawa, Y., Kawamura, M., 1990. Mechanical behaviour of rc beams damage by corrosion of reinforcement. In: Proc. 3rd International Symposium on Corrosion of Reinforcement in Concrete Construction. Wishaw, UK, pp. 178–187.

Uomoto, T., Misra, S., 1988. Behaviour of Concrete Beams and Columns in Marine Environments When Corrosion of Reinforcing Bars Takes Place. ACI Special Publication. pp. 127–145..

Vecchio, F.J., 2001. Nonlinear finite element analysis of reinforced concrete: at the crossroads? Struct. Concr. 2 (4), 201–212.